ADVANCED MATERIALS
www.advmat.de

High-Conductive Protonated Layered Oxides from H_2O Vapor-Annealed Brownmillerites

Songbai Hu, Yuanmin Zhu, Wenqiao Han, Xiaowen Li, Yanjiang Ji, Mao Ye, Cai Jin, Qi Liu, Sixia Hu, Jiaou Wang, Junling Wang, Jiaqing He, Claudio Cazorla, and Lang Chen**

Protonated 3d transition-metal oxides often display low electronic conduction, which hampers their application in electric, magnetic, thermoelectric, and catalytic fields. Electronic conduction can be enhanced by co-inserting oxygen acceptors simultaneously. However, the currently used redox approaches hinder protons and oxygen ions co-insertion due to the selective switching issues. Here, a thermal hydration strategy for systematically exploring the synthesis of conductive protonated oxides from 3d transition-metal oxides is introduced. This strategy is illustrated by synthesizing a novel layered-oxide $SrCoO_3H$ from the brownmillerite $SrCoO_{2.5}$. Compared to the insulating $SrCoO_{2.5}$, $SrCoO_3H$ exhibits an unprecedented high electronic conductivity above room temperature, water uptake at 250 °C, and a thermoelectric power factor of up to 1.2 mW K^{-2} m^{-1} at 300 K. These findings open up opportunities for creating high-conductive protonated layered oxides by protons and oxygen ions co-doping.

1. Introduction

Protonated 3d transition-metal oxides are garnering significant attention due to several unique characteristics such as giant magnetoelectric and electrochromic effects,[1–3] suppression of the thermal conductivity,[4] metal-to-insulator transition,[5,6] and proton conduction at moderate temperatures.[7–10] Despite such a wide functionality range, upon protonation the as-synthesized transition-metal oxides often display low electronic conduction, which hampers their use in electric, magnetic, and thermoelectric applications. This dearth becomes even worse for catalytic mixed ionic-electronic conductors. The currently used cathode materials for proton conducting fuel cells (PCFCs), gas sensors, or membrane reactors, although exhibit good proton or oxygen ion conduction, regrettably suffer from low intrinsic electronic conduction.[10–12] This drawback is primarily due to the fact that the insertion of protons transfers additional electrons to the metal 3d-O 2p hybridized orbital thus annihilating the hole conduction. To recover electronic conduction, one possible strategy not involving cation substitution is to co-insert an electron acceptor, for example, O ions, to neutralize the proton donated electron. However, the currently used methods, such as thermal annealing by O_2/O_3[13,14] or H_2/CO,[15,16] ionic liquid gating,[1,4] plasma implementation,[5] chemical reaction,[17] and electrochemical redox reaction,[18,19] are oxidizing and reducing incompatible at the same time. Specifically, the co-insertion of protons and oxygen ions is hindered by the redox-base selective switching. Thus, the rational design and preparation of protonated oxides with high electronic conductivity remains a big challenge.

In this report, we introduce a scalable, high-yield, and cost-efficient water-vapor annealing method to systematically create high conductive protonated oxides from oxygen-deficient transition-metal oxides. We illustrate the efficiency and technical soundness of our method by synthesizing the novel layered-oxide $SrCoO_3H$ (SCOH) from the brownmillerite $SrCoO_{3-\delta}$ (BM-SCO, $0.25 < \delta \leq 0.5$) thin film. The BM-SCO was selected because the Co-based transition-metal oxides are widely used in water-involved catalysis[9,20–24] and its structure is linked to several prosperous families of materials such as perovskite,[25] Ruddlesden-Popper,[26,27] 2H-perovskite,[28,29] and misfit-layered compounds,[30–33] which exhibit intriguing physical and chemical properties. The epitaxial thin films were phase pure, dense, and free of grain boundaries, thus provide clean platforms for exploring the ions exchange and transport kinetics. As expected, the H_2O molecules did not induce any reducing or oxidizing process and solely acted as a dopant

S. Hu, W. Han, X. Li, Y. Ji, M. Ye, C. Jin, Q. Liu, J. Wang, J. He, L. Chen
Department of Physics
Southern University of Science and Technology
Shenzhen 518055, China
E-mail: chenlang@sustech.edu.cn
Y. Zhu
School of Material Science and Engineering
Dongguan University of Technology
Dongguan 523000, China
S. Hu
SUSTech Core Research Facilities
Southern University of Science and Technology
Shenzhen 518055, China
J. Wang
Laboratory of Synchrotron Radiation
Institute of High Energy Physics
Chinese Academy of Sciences
Beijing 100039, China
C. Cazorla
Departament de Física
Universitat Politècnica de Catalunya
Campus Nord B4-B5, Barcelona E-08034, Spain
E-mail: claudio.cazorla@upc.edu

DOI: 10.1002/adma.202104623

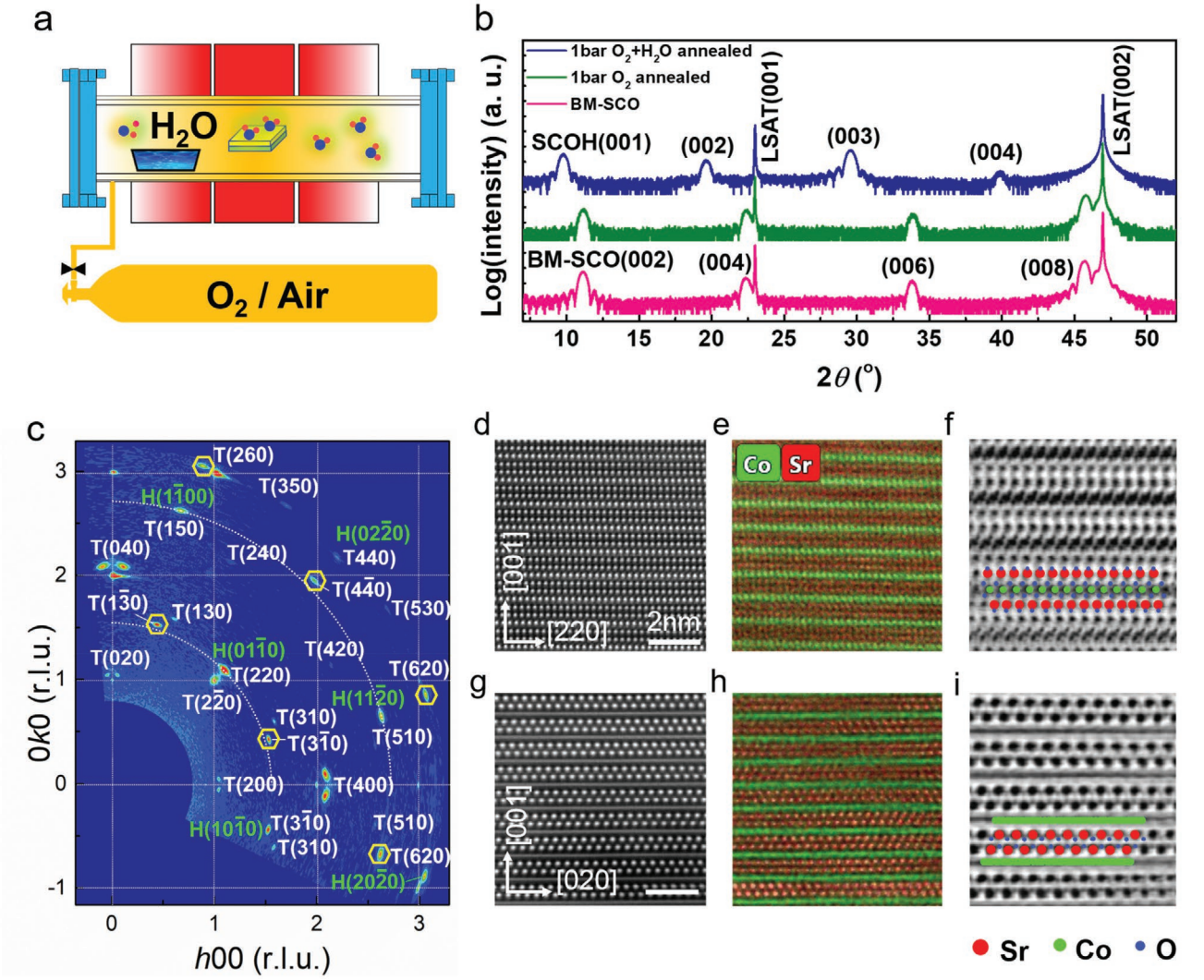

Figure 1. Preparation and structure characterization of SCOH thin films. a) A schematic view of thermal hydration on BM-SCO thin films. b) XRD θ-2θ scans of as-grown BM-SCO, 1 bar O_2 annealed and 1 bar O_2 + H_2O annealed thin films grown on LSAT substrate. c) In-plane WARSM of SCOH thin film. The q coordinates have been divided by LSAT q_{100}. The white grids corresponding to the integers h, k are guides to eyes. The T and H in the crystal plane index represent the triclinic rock salt layer (SrO) and the hexagonal layer (CoO_2), respectively. The spots of rotated CoO_2 layer are marked by hexagons. d,g) HADDF-STEM, e,h) EDS mapping, and f,i) ABF images for the SCOH (220) and (200) plane, respectively. The Sr, Co, and O atoms are painted by red, green, and blue, respectively.

source. This thermal hydration approach generates high proton concentration layered compounds that exhibit high electronic conductivity, H_2O uptake, and outstanding thermoelectric power, from the insulating BM-SCO parent phase.

2. Results and Discussion

Figure 1a schematically illustrates the thermal hydration of BM-SCO thin films. Bulk BM-SCO is orthorhombic with lattice constants of a = 5.5739 Å, b = 5.4697 Å, and c = 15.7450 Å, which can be viewed as pseudo-tetragonal (a_t = 3.905 and c_t = 7.872 Å).[34] BM-SCO is a reduced form of the perovskite $SrCoO_3$ that is characterized by columns of ordered oxygen vacancy ($V_O^{\cdot\cdot}$) along its pseudo-tetragonal [110] direction,[18,35] which offers an X-ray detectable structure feature for the oxygen evolution. As shown in Figure 1b, the sample annealed in 1 bar dry O_2 exhibited slight change compared to the as-deposited BM-SCO thin film. However, the BM-SCO completely disappeared when the sample was exposed to 1 bar wet O_2 and a new strontium cobaltite phase SCOH emerged with a significantly increased c lattice parameter (9.06 Å). The thickness of the corresponding film was ≈19 nm, and only minor changes were observed after annealing (Figure S1, Supporting Information). The transformation from BM-SCO to SCOH did not depend on the gas species (O_2 or air), only on the water vapor (Figure S2, Supporting Information). The transformation was not affected by the epitaxial strain introduced by the substrate, at least for (La,Sr)(Al,Ta)O_3 (LSAT) and $SrTiO_3$ (STO) (Figure S3, Supporting Information). The new SCOH structure resulted from a non-topotactic phase

transition[34,36,37] as the corresponding diffraction peaks did not follow those of the starting BM-SCO phase and the O_2 concentration barely impacted the transformation.

High-resolution XRD and scanning transmission electron microscopy (HR-STEM) were used to identify the SCOH structure. Figure 1c shows the in-plane wide area reciprocal space mapping (WARSM) of the SCOH thin film. A triclinic geometry with $a = b = 7.48$ Å (Figure S4, Supporting Information), $\gamma = 84°$ and its 90° rotation counterpart (Figure S5, Supporting Information) was first identified. Although all these diffractions can be indexed by this triclinic geometry, the T $(3\bar{1}0)$ and T $(1\bar{3}0)$ exhibit ten times higher intensity than their counterparts. That means they overlap with other diffractions (green labeled). These spots belong to a hexagonal-like geometry with $a = 2.90$ Å, $b = 2.82$ Å, and $\gamma = 120°$ (Figure S6, Supporting Information). Figure 1d–i presents the high-angle annular dark field (HADDF)-STEM images of SCOH (220) and (200) planes as well as the corresponding energy-dispersive X-ray spectroscopy (EDS) mapping and annular bright field (ABF) images. According to Figure 1d,e, the SCOH consists of a bright CoO_2 atomic layer and two dark SrO atomic layers. In Figure 1f,i, the stacking of SrO layers is very much like those of rock-salt sheets in Ruddlesden-Popper Sr_2CoO_4.[26] The CoO layers are unresolvable in Figure 1g because its $(10\bar{1}0)$ plane rotates 12° in in-plane from the (200) plane of SrO layer. For the (220) plane, the ABF image in Figure 1f shows that the CoO cage is the same as the edge-sharing CoO_2 octahedra in the CdI_2-type structure. Thus, the composition of rock salt SrO layer is Sr_2O_2, whereas the hexagonal CoO layer is CoO_2. The epitaxial directions are SrO [110] ‖ CoO_2 $[01\bar{1}0]$ ‖ LSAT [110] and SrO $[1\bar{1}0]$ ‖ CoO_2 $[21\bar{3}0]$ ‖ LSAT $[1\bar{1}0]$ (Figure S4, Supporting Information). It is worthy to mention that the triclinic Sr_2O_2 and hexagonal CoO_2 can be orthogonalized by the diagonals in in-plane directions. The angles α and β of the orthogonalized SCOH are determined to be 90° and 95.5° by the fast Fourier transformation (FFT) of (220) and $(2\bar{2}0)$ plane, respectively (Figure S7, Supporting Information). The lattice parameters are summarized in Table S1 (Supporting Information). The strain between the SCOH thin film and the substrate is relaxed by the stacking fault at the interface (Figure S8, Supporting Information).

With this information, the SCOH skeleton is proposed as $[Sr_2O_2]_{2.90\times2.82\times\sin120°}[CoO_2]_{3.74\times3.74\times\sin84°}$, or $[Sr_2O_2]_{0.5}CoO_2$. Its atomic structure is shown in Figure S9 (Supporting Information), which belongs to the P2/m space symmetry group. Such an alternate stacking of layers with very differentiated geometries belongs to the so-called misfit-layered compounds.[38] Owing to the alternation of transition-metal conducting and insulating rock-salt layers in the stacking sequence, both high thermopower and low thermal conductivity develop, thus unlocking thermoelectricity from the insulating BM-SCO by thermal hydration.

Figure 2a,b evidences protons and oxygen ions co-insertion occurring during the BM-SCO to SCOH phase transition. The FTIR absorbance near 3340 nm^{-1} proves directly the existence

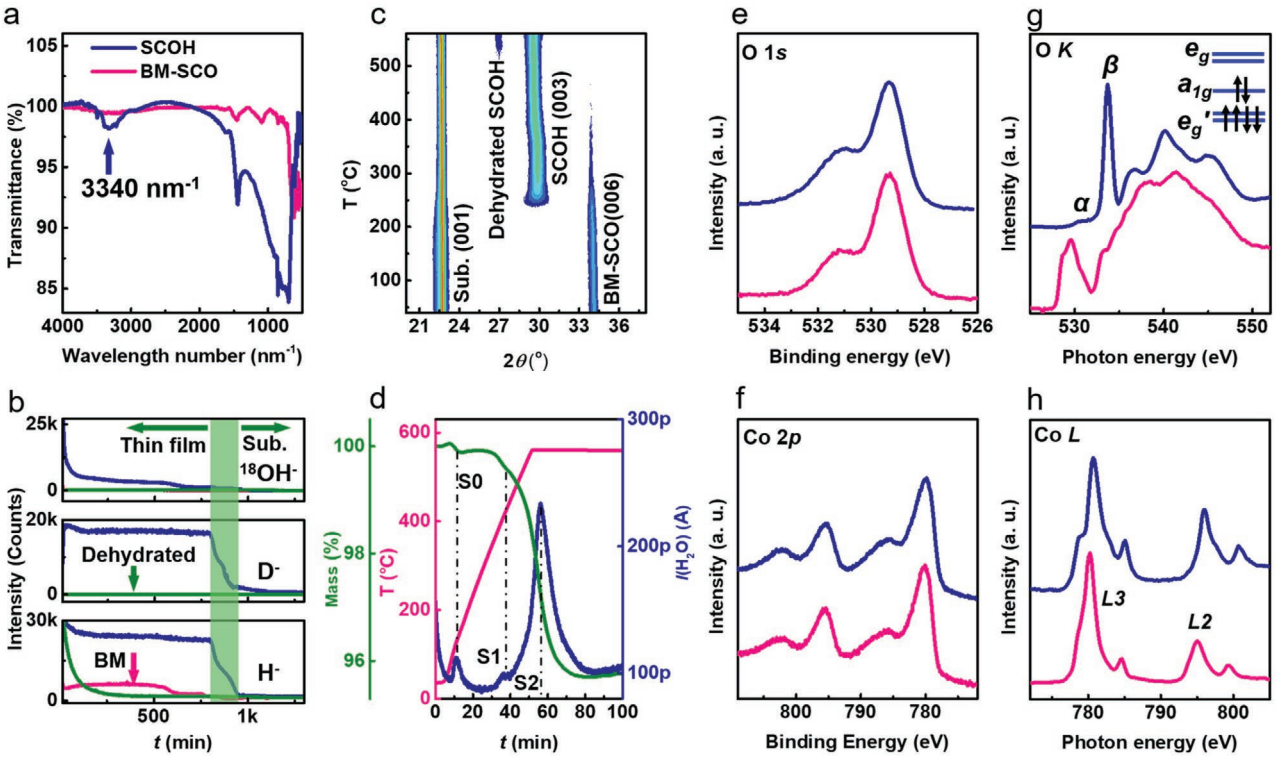

Figure 2. H_2O evolution during the BM-SCO to SCOH phase transition. a) FTIR spectroscopy of BM-SCO and SCOH powder. b) SIMS intensity depth profiles of the H^-, D^-, and $^{18}OH^-$ for H_2O, D_2O, and $H_2{}^{18}O$ vapor annealed BM-SCO thin films, respectively. The as-grown BM-SCO (pink curve) and dehydrated SCOH (olive curve) were used for comparison. The film/substrate interface is green painted. c) XRD peak evolution of BM-SCO thin film by heating the sample in wet atmosphere. d) TG-MS investigation on SCOH powder. e,f) X-ray photoelectron spectroscopy (XPS) of O 1s and Co 2p, respectively. g) X-ray absorption spectroscopy (XAS) of Co L-edge and h) O K-edge of BM-SCO and SCOH thin films.

of hydroxyl groups in SCOH. The second-ion mass spectroscopy (SIMS) depth profiles of the $H_2O/D_2O/H_2{}^{18}O$ vapor annealed thin films show that the intensity of $H^-/D^-/{}^{18}OH^-$ ions increase to thousands of counts within the film regime by annealing, and dropped to the pristine level after dehydration. The initial high and following sharp downward trend of ${}^{18}OH^-$ intensity reflects an enrichment of ${}^{18}O$ at the surface region. This is due to the layer-by-layer diffusion of O ions directed to filling the $V_O^{\cdot\cdot}$ formed in inner layers along with the phase transformation. Then the ${}^{18}O$ from $H_2{}^{18}O$ replenish the consumed O ions in the surface layer, thus they tend to accumulate within the top layers. Unlike the movement of O which is very limited in the absence of nearby $V_O^{\cdot\cdot}$, protons can always hop within the material owing to the small atomic radius. The evenly distributed H^-/D^- ions over the depth range indicates a long-distance hopping behavior for protons. The layer-by-layer conversion mode is verified in Figure S10 (Supporting Information). Therefore, we propose that both H and O ions, rather than each individual, insert into the thin film and trigger the phase transition. A variety of techniques based on redox reactions have been proposed to introduce light elements such as H or O in the BM-SCO $V_O^{\cdot\cdot}$ positions with the aim of enhancing functionality.[1,3,4,6,19,39] However, due to selective switching limitations H and O co-doping cannot be efficiently achieved through redox-based methods. Here, we have successfully doped oxygen-deficient transition-metal oxides with both H and O ions by means of water vapor annealing.

Figure 2c,d demonstrates the occurrence of H_2O evolution within SCOH by temperature-dependent XRD and thermogravimetry-mass spectroscopy (TG-MS). Under a 1 bar air atmosphere (RH ≈ 79%), the BM-SCO transformed to SCOH at ≈250 °C. At 400 °C, the SCOH (003) peak shifted slightly to the left and finally skipped to $2\theta = 27°$ at 550 °C. According to TG-MS, the stepwise increases of *c*-lattice constant then resulted from a two-stage water decomposition process. The mass reduction of 0.4% at 400 °C (S_1) and 3.8% at 550 °C (S_2) correspond to H_2O decomposition of 0.044 and 0.401 mol formula^{-1}, respectively. The S_0 peak at 117 °C came from the surface water desorption. The small S_1 hump probably was originated from residual protons hopping in the CoO_2 layers. The S_2 main peak, on the other hand, resulted from the majority of protons in the Sr_2O_2 layers at equilibrium. It is worth noting that a broadened S_2 gap is observed for the Sr_2O_2 layers corresponding to the dehydrated SCOH (Figure S11, Supporting Information), which explains the XRD peak skip at 550 °C.

Figure 2e–h describes the changes in the electronic structure before and after the phase transformation. The XPS spectra in Figure 2e,f exhibit little change for either the line shape or the peak-to-peak energy difference, which means that the cobalt ions chemical states are dominant and pretty close to Co^{3+}. The line shape of O 2p is quite similar to that of $Li_{0.94}CoO_2$.[40] The X-ray absorption spectroscopy (XAS) in Figure 2g,h, on the other hand, reflects rather different electronic configurations (Figure S12, Supporting Information) between the two. In the octahedra crystal ligand field BM-SCO, the electronic configuration of the Co^{III} 3d-O 2p hybridized orbital corresponds to a high spin state $e_g{}^2t_{2g}{}^4$.[19] In the triangular crystal field of SCOH, the small hump α that appears at low energies of O 1s spectrum arises from an electronic transition from a O 2p state to the half-filled a_{1g} state of the hybridized orbital Co^{II} 3d-O 2p in oxygen deficient SCOH. Meanwhile, the absorption at Co L-edge does not show significant sign of Co^{II}.[41] The pronounced feature β originates from an electronic transition from a O 2p state to the empty e_g state of the hybridized orbital Co^{III} 3d-O 2p[42] and the half-filled e_g state of the hybridized orbital Co^{II} 3d-O 2p. Therefore, the electronic configuration of SCOH is primarily a null spin state $e_g{}^0a_{1g}{}^2e_g'^4$ mixed with a small portion of low spin state $e_g{}^2a_{1g}{}^1e_g'^4$. Both the XPS and XAS spectra prove that there is little change in the chemical state of the Co ions after water vapor annealing, thus supporting the non-redox nature of the H_2O uptake reaction.

Based on the above analysis, the number of H in stoichiometry SCOH is fairly close to 1. The total reaction can be written as $SrCoO_{3-\delta}$ (s) + δH_2O (g) = $SrCoO_3H_2\delta$ (s) ($0.25 < \delta \leq 0.5$). It is noted that the number of inserted H_2O equals the number of $V_O^{\cdot\cdot}$ in BM-SCO. Such an equivoque correspondence can be used to accurately gauge the concentration of oxygen vacancies in nonstoichiometric oxides, n_v, which represents an important longstanding technical challenge. Conventionally, n_v is roughly estimated through XRD, XAS, or magnetization,[34,35,43] whereas here it can be accessed directly by evaluating the concentration of protons. Practically, the proton concentration is able to be controlled in the resulted materials by the number of oxygen vacancies in the perovskites parent phase. Here, by annealing BM-SCO in water vapor, we obtained the SCOH whose proton concentration is far from the defect level.

Figure 2c,d indicates a tendency for the protons to stay in the Sr_2O_2 layers. However, direct observation of the H positions is a very difficult and arduous task as demonstrated by the simulation of the corresponding STEM geometry output (Figure S13, Supporting Information). First-principles calculations based on density functional theory (DFT) were undertaken to determine the most likely H sites in the Sr_2O_2 layers. The results are shown in **Figure 3g**,h. In particular, we explored several H locations and OH^- orientations in both the SrO and CoO_2 layers. As a result of our theoretical structural searches, we found the minimum-energy stable phase reported in the paper, a metastable phase that was vibrationally and elastically stable but which possessed a higher energy than the ground state ($\Delta E \approx$ 0.4 eV fu^{-1}), and several saddle geometries for which upon structural relaxation the H atoms spontaneously moved from their initial positions in the CoO_2 or SrO layers to the final SrO positions in the metastable or stable phases (Figure S14, Supporting Information). According to our DFT calculations, the protons prefer to form hydroxyls with the O atoms in the Sr_2O_2 rather than CoO_2 layers as the latter leads to a CoOOH-like structure[22] which would attain extra *c*-lattice expansion. The hydroxyls point to the adjacent CoO_2 layers and form energetically favorable hydrogen bonds with the closest oxygen, which explains the appearance of small OH^- tilting along the [110] direction and the *a*-axis elongation of the CoO_2 layers. With the H insertion, the symmetry of SCOH reduced to space group P1.

The presence of hydrogen atoms in metal oxyhydrides in the form of hydride ions or interstitials could be possible,[44–47] hence we also analyzed them for the stable SCOH phase with DFT methods (Figure S15, Supporting Information). In particular, we evaluated the energetically most favorable positions and charge state of H interstitials in the absence and presence

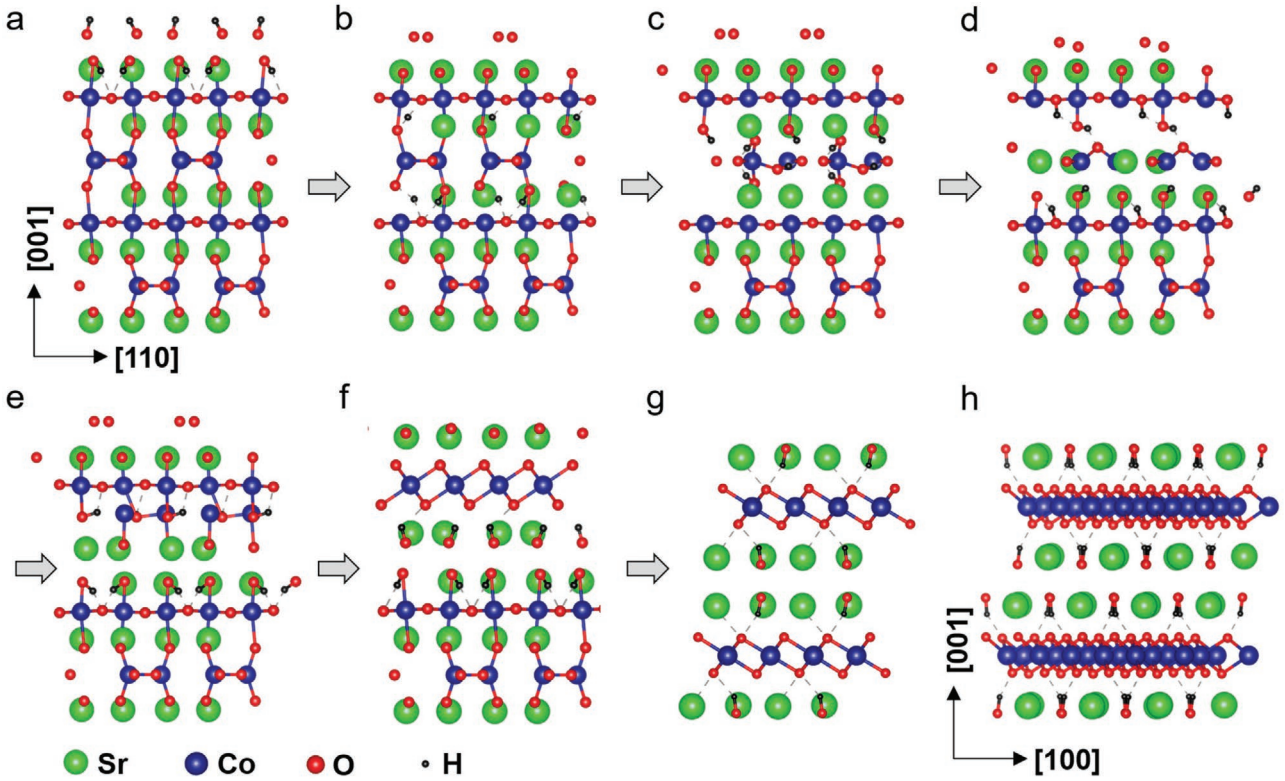

Figure 3. Water vapor-driven brownmillerite-to-layered phase transformation in strontium cobaltite thin films illustrated by seven quasi-stable intermediate states. a) H_2O absorption and dissociation on the surface BM-SCO. b) Protons hop to the O sites in SrO layer. c) The formation of hydroxyl unlocks Sr from the SrO matrix. d) Sr atoms diffuse to the oxygen vacancies in tetrahedra CoO_2 layer. e) Co atoms diffuse to the previous Sr vacancies in SrO layer. In consequence, the Sr and Co atoms exchange their sits between layers. f) Two Co layers and their neighboring O atoms transform to the CdI_2-type CoO_2 octahedra. Meanwhile, the O from H_2O intercalates into the oxygen vacancy in the surface SrO layer. g) The (110) and h) (100) planes of the resulted SCOH.

of O vacancies (in the latter case, created only in SrO layers). For the case of an H interstitial, it is found that the energetically most favorable position corresponds to the CoO_2 layer where the H atom tends to form a chemical bond with an exposed O atom. According to our DFT calculations, the charge state of such a hydrogen interstitial is H_i^- (i.e., it presents an excess of electronic charge as compared to that of the H atoms in stoichiometric SCOH). For the case of an O vacancy created in a SrO layer, it is found that the energetically most favorable position of the isolated H atom is that of the absent oxygen atom (H_O). In this case, according to our DFT calculations the charge state of such hydrogen atom is H_O^+ (i.e., it presents a deficiency of electronic charge as compared to that of the H atoms in stoichiometric SCOH).

The DFT calculations show that the energetically most favorable position for hydrogen ions in SrO layer and CoO_2 layer are H_O^+ and H_i^- in CoO_2, respectively. For the presence of H_i^- in CoO_2 layer, we think that from a sample preparation point of view the chance is very small. SCOH was prepared by annealing the sample in oxidizing O_2(1 bar) + H_2O, while the metal oxyhydrides were usually prepared by annealing with reducing CaH_2. In an O_2-rich environment, both the significant reduction of protons from H_2O to hydride ion and the survival of hydride ions at the preparation temperature (450 °C) would be rather difficult. It is noticed that the hydride ions in oxyhydrides were thermolabile when heating even in inert gas and the resulted anion-deficient structure was vulnerable to O_2.[47] The presence of H_i^- in SCOH might be possible by additional post-treatment, but less likely to exist in the as-grown state. On the other hand, the presence of H_O^+ in SrO layer is more possible. As depicted in Figure S15 (Supporting Information), the composition of SCOH would be $SrCoO_{2.5}H$ if half of O atoms in SrO layer were replaced by the H_O^+, and the Co^{3+} in $SrCoO_3H$ would be reduced to Co^{2+}. However, the amount of Co^{2+} in the as-prepared sample is negligible according to the XAS in Figure 2.

The atomistic mechanism involved in the non-topotactic protonation of BM-SCO during the thermal hydration is proposed to consist of several cations exchanges mediated by $V_O^{\cdot\cdot}$, as represented in Figure 3. First, a H_2O molecule is captured and dissociated into a OH^- and a H^+ by a metal cation (M), namely, $H_2O + MO_O^x = HO\text{-}M\text{-}O_O^xH$,[48] or by an oxygen vacancy following $H_2O + V_O^{\cdot\cdot} + O_O^x = 2OH_O^{\cdot}$, where the O_O^x and $OH_O^{\cdot}$ represent the lattice O and hydroxyl, respectively[49] (Figure 3a). At elevated temperatures, the protons are able to hop to the inner SrO layers and form hydroxyl bonds (Figure 3b). Each hydroxyl bond unlocks a Sr ion from the SrO layer (Figure 3c), which diffuses to a $V_O^{\cdot\cdot}$ position in the CoO_2 tetrahedra layer along the [111] direction (Figure 3d), thus forming a Sr vacancy (V''_{sr}). Subsequently, a Co ion diffuses to (V''_{sr}) (Figure 3e) so

that the Sr and Co cations exchange their sites through a $V_O^{\cdot\cdot}$. Then two layers of Co ions and three layers of O ions transform to one CdI_2-type CoO_2 layer. Meanwhile, the dangling O from H_2O inserts to the as-formed surface $V_O^{\cdot\cdot}$ (Figure 3f). Both the proton and oxygen ions from the H_2O molecule are thus incorporated into the newly formed $[Sr_2O_2H_2]_{0.5}CoO_2$ lattice. As the reaction proceeds, the inner BM-SCO layers repeat phase transformation steps (a)–(f) in Figure 3 using the O ions and protons transported by the top SCOH layer. The continuous uptake of H_2O by the layered $[Sr_2O_2]_{0.5}CoO_2$ makes it a potential candidate for being a mixed protonic-electronic conducting oxide.[10–12] By means of DFT methods, we estimated the total energy of the system during each phase transformation step (Figure S16, Supporting Information). Our DFT results show that the BM-SCO to $[Sr_2O_2H_2]_{0.5}CoO_2$ reaction mechanism is overall downhill made the exception of step 3 → 4 in which the Sr ions diffuse toward the $V_O^{\cdot\cdot}$ positions. This partial outcome was physically expected as Sr possesses the largest ionic radius. Meanwhile, the corresponding in-plane symmetry change and atoms rearrangement of both SrO and CoO_2 layers during the hydration are shown in Figure S17 (Supporting Information).

From the previous analysis, it is shown that the presence of $V_O^{\cdot\cdot}$ is a necessary condition for the water vapor-driven phase transformation to proceed. Further tests were undertaken to prove this point. For instance, we treated the perovskite $SrCoO_{3-\delta}$ (P-SCO, $0.25 \leq \delta < 0$) under a 1 bar O_2 + H_2O atmosphere and observed that the thin film was completely transformed to SCOH (Figure S18, Supporting Information). This occurred because in a relatively low oxygen concentration atmosphere the P-SCO was appropriately transformed to BM-SCO.[39] However, when the BM-SCO thin film was annealed in a 10 bar O_2 + H_2O atmosphere, only a part of the thin film transformed to SCOH (Figure S19, Supporting Information) due to the fact that in a high oxygen concentration atmosphere the $V_O^{\cdot\cdot}$ in BM-SCO are occupied by O atoms.[14]

Figure 4 shows the characterization of BM-SCO before and after thermal hydration. The temperature-dependent resistivity in Figure 4a demonstrates that the SCOH thin film is semimetallic between 2 and 300 K. The conductivity increases in at least four orders of magnitude as compared to that of the parent BM-SCO. Different from the ionic liquid gating,[1] the insertion of protons into 3d transition-metal oxide BM-SCO through H_2O vapor annealing does not harm the electrical conduction but yields highly conductive layered oxides. Figure 4b shows the experimental Seebeck coefficient of BM-SCO and SCOH over the temperature interval 400–10 K. The *S* positive sign implies that both BM-SCO and SCOH are p-type conductors. Although the conductivity increases significantly, the *S* coefficient of SCOH only decreases slightly. Figure 4c shows that at 300 K the power factor of SCOH is significantly improved than that of BM-SCO, thus demonstrating a marked increase in the electrical conductivity while retaining excellent thermoelectric power. At room temperature, the power factor of SCOH attains the value 1.2 mW K^{-2} m^{-1}, which is ≈5 times larger than that

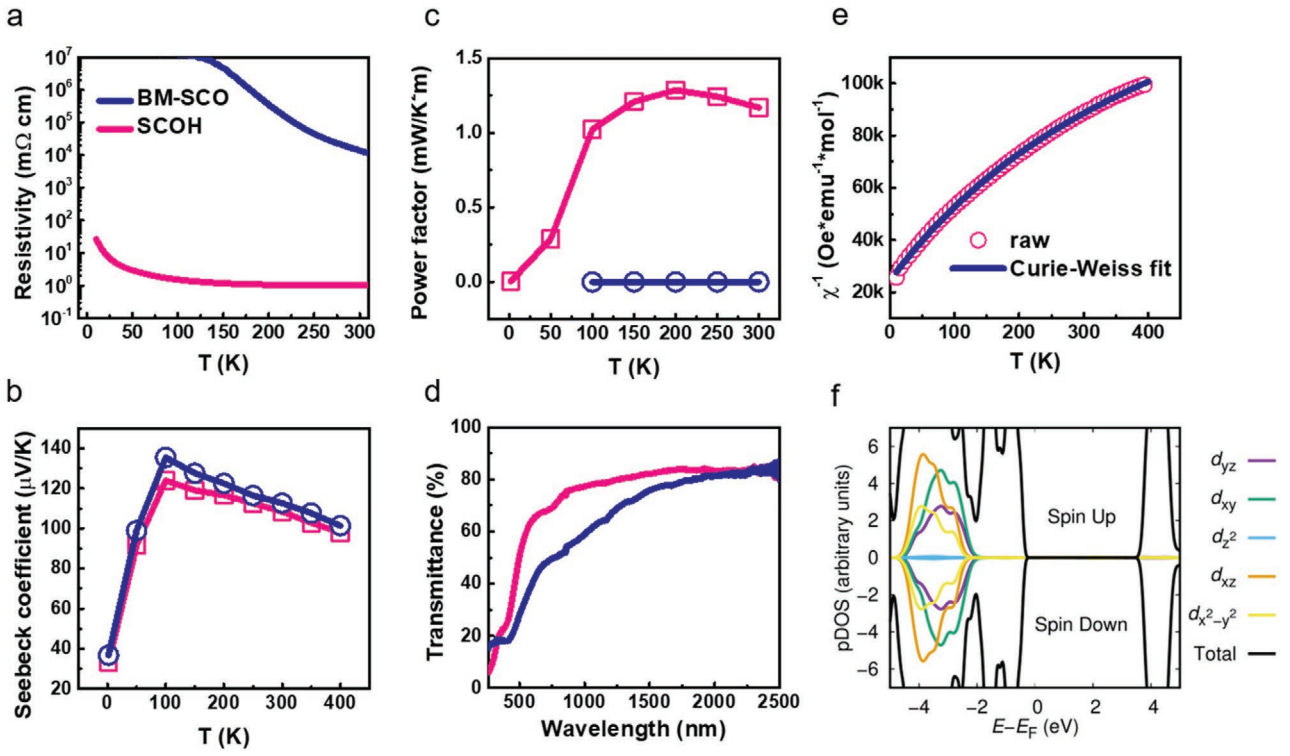

Figure 4. Properties of BM-SCO thin films before and after thermal hydration. a) Temperature-dependent resistivity, b) Seebeck coefficient, c) thermoelectric power factor, d) optical transmittance, e) inversed magnetic susceptibility versus temperature of BM-SCO and SCOH. f) Total and partial Co d densities of electronic states calculated with DFT methods for bulk SCOH. Spin up and spin down densities of electronic states are represented along the positive and negative sections of the ordinate axis, respectively. Results were obtained for the ground-state and the null-spin solution was found to render the lowest total energy in the spin-polarized DFT calculations based in the range-separated hybrid HSE06 functional.

of the widely studied $Ca_3Co_4O_9$ thin films.[50] These numbers show that layered SCOH, although protonated, is high-conductive and an outstanding thermoelectric oxide material.[51–54] The optical transmittance in Figure 4d shows that the transparency of the SCOH thin film stabilizes at 80% in the infrared light range and improves up to 20% in the visible light range than that of the BM-SCO. The absorption edge shifts to the violet side, and the optical bandgap is estimated to be 2.61 eV which is 0.33 eV wider than the BM-SCO. Combined with the thermoelectricity, the transparent semi-metallic SCOH thin film exhibits great potential for hybrid energy harvesting such as transparent conductive window and thermoelectric solar cells.

The inverse magnetic susceptibility (χ) of SCOH is shown in Figure 4e as a function of temperature. Between 2 and 400 K, the measured data are well described by the Curie–Weiss law using the $\chi = \chi_0 + C/(T-\theta)$, where χ_0 is a temperature independent contribution. The Curie constant C is fitted to be 0.023. Using the $C \approx n(n+2)/8$,[55] the unpaired electrons n is calculated to be 0.09 ($S \approx 0$), which well agrees with the XAS results. From our spin-polarized DFT calculations, it was found that for the lowest-energy state the Co electrons arrange over the d orbitals according to a low-spin (LS) state characterized by null Co magnetic moments (Figure 4f). In particular, the energy of the Co LS state was estimated to be 45 meV fu^{-1} below that of the corresponding Co high-spin (HS) state (for both possible ferromagnetic and antiferromagnetic spin structures). This theoretical outcome is in consistent agreement with our experimental measurements. We note that the impact of the selected U parameter value on our DFT results was carefully investigated (Figure S20, Supporting Information). Therefore, based on our experiments and DFT calculations we can conclude that SCOH is a nonmagnetic semi-metal.

3. Conclusion

In summary, we used the H_2O vapor to anneal the BM-SCO thin film and thus synthesize a novel protonated layered-oxide SCOH, which exhibited H_2O uptake at 250 °C, high electronic conductivity, thermoelectricity, optical transparency, and lack of magnetism, in stark contrast with the parent phase. We demonstrated that the uptake of water into the thin film drove the bulk-to-layered phase transformation and proposed a proton-triggered cation exchange mechanism mediated by the presence of oxygen vacancies to explain the unravelled non-topotactic phase transition. The resulting material may be a good candidate for electrodes of thermoelectric PCFCs, thermoelectric solar cells, or transparent conductive window that boosts synergistic energy harvesting.[56] Our work shows the great potential of hydrogen and oxygen co-doping in reconstructing 3d transition-metal oxides for advanced energy conversion, and the use of thin film as a clean platform to study the exchange and transport of ions in transition-metal oxides. Thus, the acid-base ions co-insertion method introduced here overcomes the selective switching issues typically found in redox reaction-based approaches, and it is sufficiently general to allow for the synthesis of a new class of proton-containing multifunctional oxide materials from brownmillerites such as $CaFeO_{2.5}$, $CaCoO_{2.5}$, and $GaInO_{2.5}$, or any oxygen-deficient oxides such as WO_x, VO_x, TiO_x, $BaCoO_{3-\delta}$, or $SrNiO_{3-\delta}$.

4. Experimental Section

Sample Preparation: The BM-SCO thin films were deposited on LSAT or STO by pulsed laser deposition (PLD). The growth conditions were a temperature of 700–800 °C, oxygen pressure of 13 Pa, laser energy density of 1.5 J cm^{-2}, and laser frequency of 6 Hz. The film thickness is ≈20 nm for 1200 pulses deposition. The P-SCO thin films were obtained by doing an in situ post annealing in an oxygen pressure of 90 000 Pa at 650 °C for 30 min. The as-grown thin films were then annealed in a H_2O (or D_2O, $H_2{}^{18}O$) vapor atmosphere. The base pressure (O_2/air) was controlled at 1 bar. At 450 °C the evaporated water promoted the pressure to almost double of the initial. The sample was cooled down naturally after 1 h annealing at 450 °C. The SCOH thin films were dehydrated by annealing the sample at 550 °C in air for 1 h. The BM-SCO powder was made by solid-state reaction from $SrCO_3$ and Co_3O_4 powder with 3:1 molar ratio. After 24 h of sintering in air at 1200 °C the sample was quenched to room temperature by liquid nitrogen. By repeating the process, the BM-SCO powder without impurity was obtained. The SCOH powder was made by annealing the BM-SCO powder in 10 bar O_2+H_2O for 24 h. The vapor pressure was ≈50 bar at 800 °C. Then the sample was cooled down to 150 °C naturally and took out. The high temperature and pressure were used to improve the crystallinity.

Sample Characterization: The sample structure was characterized by a high-resolution X-ray diffractometer (Rigaku SmartLab). The high temperature XRD was carried out using a domed hot stage (Anton Paar, DHS 1100) in an ambient atmosphere (air, RH ≈ 79%). HAADF-STEM and EDS were conducted using a double aberration-corrected transmission electron microscopy (Thermo Fisher Themis Z G2 60–300) operated at 300 kV. The powder FTIR was collected with a Thermo is50/6700 spectrometer. The SIMS was obtained using an instrument Cameca IMS4f. D_2O was used to exclude the possible absorption H_2O on the surface. $H_2{}^{18}O$ was also used to trace the oxygen evolution. The TG-MS was investigated using a Netzsch STA449C + QMS 403D Aeolos analyzer. The feeding gas was dry air at a rate of 5 mL min^{-1}. The XPS was obtained using a ThermoFisher Scientific ESCALAB 250 photoelectron spectrometer with an Al Kα source. The XAS was taken at beamline 4B9B of Beijing Synchrotron Radiation Facility in the total fluorescence yield (TFY) mode. The resistivity and Seebeck coefficient of the thin films were measured using a Quantum Design PPMS in a four-probe method. The room temperature Seebeck coefficient was verified using a portable thermoelectric monitor (PTM-3, JouleYacht, China). The resistance of BM-SCO was measured by a Keithley 6517B picometer with a two-probe connection. The optical transmittance of SCOH thin film was obtained by a Perklin Elmer Lambda 750 spectrometer. The absorbance of LSAT was subtracted by using two sides polished bare substrate. The magnetization of SCOH powder was measured with a Quantum Designed MPMS3.

First-Principles Calculations: Spin-polarized DFT[57] calculations were performed to theoretically characterize the structural, vibrational, mechanical, and electronic properties of SCOH. The ground-state SCOH geometry determined with theoretical DFT methods, which is fully consistent with the structural data obtained from the experiments, was found to be both mechanically and vibrationally stable (Figure S21, Supporting Information). The PBEsol functional[58] was used as implemented in the VASP software.[59] A "Hubbard-U" scheme[60] with U = 4 eV was used in most calculations for a better treatment of the localized Co 3d electronic orbitals.[61] Several tests were performed to assess the impact of the selected U parameter value on the final DFT results (Figure S18, Supporting Information). The "projector augmented wave" method was used to represent the ionic cores[62] by considering the following electrons as valence: Sr 4s, 4p, and 5s; Co 3d and 4s; O 2s and 2p; H 1s. Wave functions were represented in a plane-wave basis truncated at 650 eV. For integrations within the first Brillouin zone,

thick Monkhorst-Pack k-point grids with a density equivalent to that of $16 \times 16 \times 16$ for a conventional five-atom perovskite unit cell were used. Periodic boundary conditions were applied along the three lattice vectors of the simulation supercell. Geometry relaxations were performed with a conjugate-gradient algorithm that optimized the ionic positions and the volume and shape of the simulation cell. The relaxations were halted when the forces in the atoms were all below 0.005 eV $Å^{-1}$. By using these technical parameters, the obtained energies were converged to within 0.5 meV fu^{-1}. Different possible spin magnetic arrangements involving the electronic Co d orbitals (i.e., ferromagnetic and antiferromagnetic type "A" and "G"[63]) were explored in DFT calculations. For the calculation of electronic densities of states, the more accurate range-separated hybrid functional HSE06 was used.[64] For phonon frequency calculations, the so-called "direct approach"[64] was used, in which the force-constant matrix of the crystal was directly calculated in real-space by considering the proportionality between the atomic displacements and forces when the former is sufficiently small (in this case this condition was satisfied with atomic displacements of 0.02 Å). Large supercells containing 192 atoms were used in the calculations to guarantee that the elements of the force-constant matrix had all fallen off to negligible values at their boundaries, a condition that follows from the use of periodic boundary conditions. A dense k-point grid of $3 \times 3 \times 3$ for the calculation of the atomic forces with VASP was used. The computation of the non-local parts of the pseudopotential contributions was performed in reciprocal space to maximize the numerical accuracy. Once the force-constant matrix was determined, it was Fourier transformed to obtain the phonon spectrum at any q point contained in the BZ. This step was performed with the PHON code,[65] in which the translational invariance of the system (to impose that the three acoustic branches were exactly zero at the Γ point) was exploited and central differences in the atomic forces (i.e., positive and negative atomic displacements were considered) were used. A complete phonon calculation involved the evaluation of atomic forces for 144 different configurations by using the computational parameters just described.

Supporting Information

Supporting Information is available from the Wiley Online Library or from the author.

Acknowledgements

S.H. and Y.Z. contributed equally to this work. The authors acknowledge support by the National Natural Science Foundation of China (Grant Nos. 11804145 and 12004156), the Science and Technology Research Items of Shenzhen (Grant Nos. JCYJ20190809142603695, JCYJ20180504165650580, and JCYJ20190809181601639), and High-level Special Funding (Nos. G02206303 and G02206403). Computational resources and technical assistance were provided by the Australian Government and the Government of Western Australia through the National Computational Infrastructure (NCI) and Magnus under the National Computational Merit Allocation Scheme and the Pawsey Supercomputing Centre. C.C. acknowledges support from the Spanish Ministry of Science, Innovation, and Universities under the "Ramón y Cajal" fellowship RYC2018-024947-I. The authors would like to acknowledge Dr. F. Zhang for the great help on the SIMS measurement and technical support from SUSTech CRF.

Conflict of Interest

The authors declare no conflict of interest.

Data Availability Statement

Research data are not shared.

Keywords

brownmillerite, conductivity, layered oxides, protons, water vapor

Received: June 16, 2021
Revised: August 13, 2021
Published online:

[1] N. Lu, P. Zhang, Q. Zhang, R. Qiao, Q. He, H.-B. Li, Y. Wang, J. Guo, D. Zhang, Z. Duan, Z. Li, M. Wang, S. Yang, M. Yan, E. Arenholz, S. Zhou, W. Yang, L. Gu, C.-W. Nan, J. Wu, Y. Tokura, P. Yu, *Nature* **2017**, *546*, 124.
[2] M. Wang, X. Sui, Y. Wang, Y.-H. Juan, Y. Lyu, H. Peng, T. Huang, S. Shen, C. Guo, J. Zhang, Z. Li, H.-B. Li, N. Lu, A. T. N'Diaye, E. Arenholz, S. Zhou, Q. He, Y.-H. Chu, W. Duan, P. Yu, *Adv. Mater.* **2019**, *31*, 1900458.
[3] H.-B. Li, F. Lou, Y. Wang, Y. Zhang, Q. Zhang, D. Wu, Z. Li, M. Wang, T. Huang, Y. Lyu, J. Guo, T. Chen, Y. Wu, E. Arenholz, N. Lu, N. Wang, Q. He, L. Gu, J. Zhu, C.-W. Nan, X. Zhong, H. Xiang, P. Yu, *Adv. Sci.* **2019**, *6*, 1901432.
[4] Q. Lu, S. Huberman, H. Zhang, Q. Song, J. Wang, G. Vardar, A. Hunt, I. Waluyo, G. Chen, B. Yildiz, *Nat. Mater.* **2020**, *19*, 655.
[5] S. Chen, H. Zhou, X. Ye, Z. Chen, J. Zhao, S. Das, C. Klewe, L. Zhang, E. Lupi, P. Shafer, E. Arenholz, D. Jin, H. Huang, Y. Lu, X. Li, M. Wu, S. Ke, H. Xu, X. Zeng, C. Huang, L. W. Martin, L. Chen, *Adv. Funct. Mater.* **2019**, *29*, 1907072.
[6] T. Katayama, A. Chikamatsu, H. Kamisaka, Y. Yokoyama, Y. Hirata, H. Wadati, T. Fukumura, T. Hasegawa, *AIP Adv.* **2015**, *5*, 107147.
[7] H. Iwahara, *Solid State Ionics* **1996**, *86–88*, 9.
[8] L. Malavasi, C. A. J. Fisher, M. S. Islam, *Chem. Soc. Rev.* **2010**, *39*, 4370.
[9] E. Vollestad, R. Strandbakke, M. Tarach, D. Catalan-Martinez, M. L. Fontaine, D. Beeaff, D. R. Clark, J. M. Serra, T. Norby, *Nat. Mater.* **2019**, *18*, 752.
[10] M. Papac, V. Stevanović, A. Zakutayev, R. O'Hayre, *Nat. Mater.* **2021**, *20*, 301.
[11] A. Grimaud, F. Mauvy, J. M. Bassat, S. Fourcade, L. Rocheron, M. Marrony, J. C. Grenier, *J. Electrochem. Soc.* **2012**, *159*, B683.
[12] C. Duan, J. Huang, N. Sullivan, R. O'Hayre, *Appl. Phys. Rev.* **2020**, *7*, 011314.
[13] J. R. Petrie, C. Mitra, H. Jeen, W. S. Choi, T. L. Meyer, F. A. Reboredo, J. W. Freeland, G. Eres, H. N. Lee, *Adv. Funct. Mater.* **2016**, *26*, 1564.
[14] S. B. Hu, Y. Wang, C. Cazorla, J. Seidel, *Chem. Mater.* **2017**, *29*, 708.
[15] D. Li, K. Lee, B. Y. Wang, M. Osada, S. Crossley, H. R. Lee, Y. Cui, Y. Hikita, H. Y. Hwang, *Nature* **2019**, *572*, 624.
[16] C. M. Folkman, S. H. Chang, H. Jeen, E. Perret, P. M. Baldo, C. Thompson, J. A. Eastman, H. N. Lee, D. D. Fong, *APL Mater.* **2019**, *7*, 081126.
[17] N. Ichikawa, M. Iwanowska, M. Kawai, C. Calers, W. Paulus, Y. Shimakawa, *Dalton Trans.* **2012**, *41*, 10507.
[18] A. Nemudry, P. Rudolf, R. Schöllhorn, *Chem. Mater.* **1996**, *8*, 2232.
[19] S. Hu, W. Han, S. Hu, J. Seidel, J. Wang, R. Wu, J. Wang, J. Zhao, Z. Xu, M. Ye, L. Chen, *Chem. Mater.* **2019**, *31*, 6117.
[20] W. Zhou, J. Sunarso, M. Zhao, F. Liang, T. Klande, A. Feldhoff, *Angew. Chem., Int. Ed.* **2013**, *52*, 14036.
[21] Y. Zhu, L. Zhang, B. Zhao, H. Chen, X. Liu, R. Zhao, X. Wang, J. Liu, Y. Chen, M. Liu, *Adv. Funct. Mater.* **2019**, *29*, 1901783.

[22] A. Bergmann, T. E. Jones, E. M. Moreno, D. Teschner, P. Chernev, M. Gliech, T. Reier, H. Dau, P. Strasser, *Nat. Catal.* **2018**, *1*, 711.
[23] B. Han, K. A. Stoerzinger, V. Tileli, A. D. Gamalski, E. A. Stach, Y. Shao-Horn, *Nat. Mater.* **2017**, *16*, 121.
[24] C. Duan, J. Tong, M. Shang, S. Nikodemski, M. Sanders, S. Ricote, A. Almansoori, R. O'Hayre, *Science* **2015**, *349*, 1321.
[25] Y. Long, Y. Kaneko, S. Ishiwata, Y. Taguchi, Y. Tokura, *J. Phys.: Condens. Matter* **2011**, *23*, 245601.
[26] X. L. Wang, H. Sakurai, E. Takayama-Muromachi, *J. Appl. Phys.* **2005**, *97*, 10M519.
[27] R. M. Helps, N. H. Rees, M. A. Hayward, *Inorg. Chem.* **2010**, *49*, 11062.
[28] W. T. A. Harrison, S. L. Hegwood, A. J. Jacobson, *J. Chem. Soc., Chem. Commun.* **1995**, *19*, 1953.
[29] Q. Zhao, J. Darriet, M.-H. Whangbo, L. Ye, C. Stackhouse, H.-C. zur Loye, *J. Am. Chem. Soc.* **2011**, *133*, 20981.
[30] K. Takahata, Y. Iguchi, D. Tanaka, T. Itoh, I. Terasaki, *Phys. Rev. B* **2000**, *61*, 12551.
[31] D. Pelloquin, S. Hébert, A. Maignan, B. Raveau, *Solid State Sci.* **2004**, *6*, 167.
[32] C. de Vaulx, M. H. Julien, C. Berthier, M. Horvatic, P. Bordet, V. Simonet, D. P. Chen, C. T. Lin, *Phys. Rev. Lett.* **2005**, *95*, 186405.
[33] B. Višić, L. S. Panchakarla, R. Tenne, *J. Am. Chem. Soc.* **2017**, *139*, 12865.
[34] H. Jeen, W. S. Choi, J. W. Freeland, H. Ohta, C. U. Jung, H. N. Lee, *Adv. Mater.* **2013**, *25*, 3651.
[35] Y. Takeda, R. Kanno, T. Takada, O. Yamamoto, M. Takano, Y. Bando, *Z. Anorg. Allg. Chem.* **1986**, *9–10*, 259.
[36] L. Cao, O. Petracic, P. Zakalek, A. Weber, U. Rücker, J. Schubert, A. Koutsioubas, S. Mattauch, T. Brückel, *Adv. Mater.* **2019**, *31*, 1806183.
[37] A. Khare, D. Shin, T. S. Yoo, M. Kim, T. D. Kang, J. Lee, S. Roh, I.-H. Jung, J. Hwang, S. W. Kim, T. W. Noh, H. Ohta, W. S. Choi, *Adv. Mater.* **2017**, *29*, 1606566.
[38] A. C. Masset, C. Michel, A. Maignan, M. Hervieu, O. Toulemonde, F. Studer, B. Raveau, J. Hejtmanek, *Phys. Rev. B* **2000**, *62*, 166.
[39] H. Jeen, W. S. Choi, M. D. Biegalski, C. M. Folkman, I. C. Tung, D. D. Fong, J. W. Freeland, D. Shin, H. Ohta, M. F. Chisholm, H. N. Lee, *Nat. Mater.* **2013**, *12*, 1057.
[40] L. Dahéron, R. Dedryvère, H. Martinez, M. Ménétrier, C. Denage, C. Delmas, D. Gonbeau, *Chem. Mater.* **2008**, *20*, 583.
[41] L. Gao, X. Chen, X. Lyu, G. Ji, Z. Chen, M. Zhu, X. Cao, C. Li, A. Ji, Z. Cao, N. Lu, *J. Phys.: Condens. Matter* **2021**, *33*, 104004.
[42] T. Mizokawa, Y. Wakisaka, T. Sudayama, C. Iwai, K. Miyoshi, J. Takeuchi, H. Wadati, D. G. Hawthorn, T. Z. Regier, G. A. Sawatzky, *Phys. Rev. Lett.* **2013**, *111*, 056404.
[43] H. Taguchi, M. Shimada, M. Koizumi, *J. Solid State Chem.* **1979**, *29*, 221.
[44] E. J. C. M. A. Hayward, J. B. Claridge, M. Bieringer, M. J. Rosseinsky, C. J. Kiely, S. J. Blundell, I. M. Marshall, F. L. Pratt, *Science* **2002**, *295*, 1882.
[45] Y. Kobayashi, O. J. Hernandez, T. Sakaguchi, T. Yajima, T. Roisnel, Y. Tsujimoto, M. Morita, Y. Noda, Y. Mogami, A. Kitada, M. Ohkura, S. Hosokawa, Z. Li, K. Hayashi, Y. Kusano, J. Kim, N. Tsuji, A. Fujiwara, Y. Matsushita, K. Yoshimura, K. Takegoshi, M. Inoue, M. Takano, H. Kageyama, *Nat. Mater.* **2012**, *11*, 507.
[46] J. Luo, J.-H. Im, M. T. Mayer, M. Schreier, M. K. Nazeeruddin, N.-G. Park, S. D. Tilley, H. J. Fan, M. Graetzel, *Science* **2014**, *345*, 1593.
[47] N. Masuda, Y. Kobayashi, O. Hernandez, T. Bataille, S. Paofai, H. Suzuki, C. Ritter, N. Ichijo, Y. Noda, K. Takegoshi, C. Tassel, T. Yamamoto, H. Kageyama, *J. Am. Chem. Soc.* **2015**, *137*, 15315.
[48] D. K. Bediako, Y. Surendranath, D. G. Nocera, *J. Am. Chem. Soc.* **2013**, *135*, 3662.
[49] D. Poetzsch, R. Merkle, J. Maier, *Adv. Funct. Mater.* **2015**, *25*, 1542.
[50] B. Paul, E. M. Bjork, A. Kumar, J. Lu, P. Eklund, *ACS Appl. Energy Mater.* **2018**, *1*, 2261.
[51] Z. Ma, J. Wei, P. Song, M. Zhang, L. Yang, J. Ma, W. Liu, F. Yang, X. Wang, *Mater. Sci. Semicond. Process.* **2021**, *121*, 105303.
[52] N. Nandihalli, C.-J. Liu, T. Mori, *Nano Energy* **2020**, *78*, 105186.
[53] X.-L. Shi, W.-Y. Chen, X. Tao, J. Zou, Z.-G. Chen, *Mater. Horiz.* **2020**, *7*, 3065.
[54] X.-L. Shi, H. Wu, Q. Liu, W. Zhou, S. Lu, Z. Shao, M. Dargusch, Z.-G. Chen, *Nano Energy* **2020**, *78*, 105195.
[55] Ph. Boullay, R. Seshadri, F. Studer, M. Hervieu, D. Groult, B. Raveau, *Chem. Mater.* **1998**, *10*, 92.
[56] F. Bonaccorso, L. Colombo, G. Yu, M. Stoller, V. Tozzini, A. C. Ferrari, R. S. Ruoff, V. Pellegrini, *Science* **2015**, *347*, 1246501.
[57] C. Cazorla, J. Boronat, *Rev. Mod. Phys.* **2017**, *89*, 035003.
[58] J. P. Perdew, A. Ruzsinszky, G. I. Csonka, O. A. Vydrov, G. E. Scuseria, L. A. Constantin, X. Zhou, K. Burke, *Phys. Rev. Lett.* **2008**, *100*, 136406.
[59] G. Kresse, J. Furthmüller, *Phys. Rev. B* **1996**, *54*, 11169.
[60] S. L. Dudarev, G. A. Botton, S. Y. Savrasov, C. J. Humphreys, A. P. Sutton, *Phys. Rev. B* **1998**, *57*, 1505.
[61] P. Rivero, C. Cazorla, *Phys. Chem. Chem. Phys.* **2016**, *18*, 30686.
[62] P. E. Blochl, *Phys. Rev. B* **1994**, *50*, 17953.
[63] C. Cazorla, O. Dieguez, J. Iniguez, *Sci. Adv.* **2017**, *3*, e1700288.
[64] J. Heyd, G. E. Scuseria, M. Ernzerhof, *J. Chem. Phys.* **2003**, *118*, 8207.
[65] D. Alfe, *Comput. Phys. Commun.* **2009**, *180*, 2622.